CORA Cork Open Research Archive
Cartlann Taighde Oscailte Chorcaí

Title	Epitaxial growth of antimony nanofilms on HOPG and thermal desorption to control the film thickness
Authors	Xing, Shuya;Lei, Le;Dong, Haoyu;Guo, Jianfeng;Cao, Feiyue;Gu, Shangzhi;Hussain, Sabir;Pang, Fei;Ji, Wei;Xu, Rui;Cheng, Zhihai
Publication date	2020-07-03
Original Citation	Xing, S., Lei, L., Dong, H., Guo, J., Cao, F., Gu, S., Hussain, S., Pang, F., Ji, W., Xu, R. and Cheng, Z. (2020) 'Epitaxial growth of antimony nanofilms on HOPG and thermal desorption to control the film thickness*', Chinese Physics B, 29(9), p. 096801. Available at: https://doi.org/10.1088/1674-1056/aba27c
Type of publication	Article (peer-reviewed);Article
Link to publisher's version	https://doi.org/10.1088/1674-1056/aba27c - 10.1088/1674-1056/aba27c
Rights	© 2020 Chinese Physical Society and IOP Publishing Ltd
Download date	2026-11-16 19:17:57
Item downloaded from	https://hdl.handle.net/10468/15349

UCC
University College Cork, Ireland
Coláiste na hOllscoile Corcaigh

Chinese Physics B

RAPID COMMUNICATION

Epitaxial growth of antimony nanofilms on HOPG and thermal desorption to control the film thickness*

To cite this article: Shuya Xing *et al* 2020 *Chinese Phys. B* **29** 096801

View the article online for updates and enhancements.

This content was downloaded from IP address 124.16.156.115 on 31/08/2020 at 04:07

RAPID COMMUNICATION

Epitaxial growth of antimony nanofilms on HOPG and thermal desorption to control the film thickness*

Shuya Xing(邢淑雅)[1], Le Lei(雷乐)[1], Haoyu Dong(董皓宇)[1], Jianfeng Guo(郭剑峰)[1], Feiyue Cao(曹飞跃)[1], Shangzhi Gu(顾尚志)[1], Sabir Hussain[2,3], Fei Pang(庞斐)[1,†], Wei Ji(季威)[1], Rui Xu(许瑞)[1], and Zhihai Cheng(程志海)[1,‡]

[1] *Beijing Key Laboratory of Optoelectronic Functional Materials & Micro-nano Devices, Department of Physics, Renmin University of China, Beijing* 100872, *China*

[2] *CAS Key Laboratory of Standardization and Measurement for Nanotechnology, CAS Center for Excellence in Nanoscience, National Center for Nanoscience and Technology, Beijing* 100190, *China*

[3] *University of Chinese Academy of Sciences, Beijing* 100039, *China*

(Received 24 May 2020; revised manuscript received 23 June 2020; accepted manuscript online 3 July 2020)

Group-V elemental nanofilms were predicted to exhibit interesting physical properties such as nontrivial topological properties due to their strong spin–orbit coupling, the quantum confinement, and surface effect. It was reported that the ultrathin Sb nanofilms can undergo a series of topological transitions as a function of the film thickness h: from a topological semimetal ($h > 7.8$ nm) to a topological insulator (7.8 nm $> h >$ 2.7 nm), then a quantum spin Hall (QSH) phase (2.7 nm $> h >$ 1.0 nm) and a topological trivial semiconductor ($h < 1.0$ nm). Here, we report a comprehensive investigation on the epitaxial growth of Sb nanofilms on highly oriented pyrolytic graphite (HOPG) substrate and the controllable thermal desorption to achieve their specific thickness. The morphology, thickness, atomic structure, and thermal-strain effect of the Sb nanofilms were characterized by a combination study of scanning electron microscopy (SEM), atomic force microscopy (AFM), and scanning tunneling microscopy (STM). The realization of Sb nanofilms with specific thickness paves the way for the further exploring their thickness-dependent topological phase transitions and exotic physical properties.

Keywords: epitaxial growth, antimony films, scanning tunneling microscope (STM), thermal desorption

PACS: 68.35.bg, 68.55.−a, 68.43.Vx, 68.37.Ef **DOI:** 10.1088/1674-1056/aba27c

1. Introduction

Two-dimensional materials show a good application prospect in many application fields, such as electronics and optoelectronics, sensors, photovoltaics, quantum dots, etc.[1] Recently, many single-element two-dimensional materials have been successfully fabricated, including borophene,[2] germanene,[3] silicene,[4] phosphorene,[5–7] tellurene,[8] and so on. Within these materials, the two-dimensional materials made of heavy elements have been theoretically predicated as exotic nontrivial topological materials due to their strong spin–orbit coupling effect. In experiments, the fabrication of antimonene,[9] bismuthine,[10] stanne,[11] etc. have been realized by different methods.

The Sb(111) single crystal is a topologically nontrivial semimetal. In the early years, the topological state of Sb(111) surface has been characterized by angle resolved photoemission spectroscopy (ARPES)[12,13] and scanning tunneling microscopy (STM).[14] Recently, it is theoretically predicted that the Sb (111) nanofilm undergoes a series of topological transitions with thickness: it transforms from a topological semimetal to a topological insulator at 7.8 nm (22 layers), and then transforms into a quantum spin phase (QSH) at 2.7 nm (8 layers), finally at 1.0 nm (3 layers) becomes a normal semiconductor (topological trivial).[15] Synthesis of high quality Sb nanofilms of various thickness is the preconditions for studying their thickness-dependent topological properties. Until now, Sb nanofilms have been mainly obtained by micromechanical exfoliation,[16] liquid phase exfoliation,[17] and van der Waals epitaxy.[18–22] In comparison, there are more advantages for the molecular beam epitaxy[23–26] method in fabricating high-purity ultrathin Sb nanofilms of specific thickness. Recently, the epitaxial growth of Sb nanofilms on the lattice matching substrates, such as Bi_2Te_3, Sb_2Te_3,[27] $PdTe_2$,[9] Ge (111),[28] and Ag (111),[29] has been reported. The topological edge states of ultrathin Sb nanofilms deposited on Si (111)[30] and Bi_2Te_2Se[31] have been observed by STM. The ARPES measurements indicated that the intrinsic electronic states of these films have been affected by the strong inter-

*Project supported by the National Natural Science Foundation of China (Grant Nos. 21622304, 61674045, 11604063, and 61911540074), the National Key Research and Development Program of China (Grant No. 2016YFA0200700), the Strategic Priority Research Program and Key Research Program of Frontier Sciences and Instrument Developing Project (Chinese Academy of Sciences, CAS) (Grant Nos. XDB30000000, QYZDB-SSW-SYS031, and YZ201418). Z. H. Cheng was supported by Distinguished Technical Talents Project and Youth Innovation Promotion Association CAS, the Fundamental Research Funds for the Central Universities, China, and the Research Funds of Renmin University of China (Grant No. 18XNLG01).

†Corresponding author. E-mail: feipang@ruc.edu.cn

‡Corresponding author. E-mail: zhihaicheng@ruc.edu.cn

© 2020 Chinese Physical Society and IOP Publishing Ltd

facial interactions between the film and substrate.[32–39] It is an appropriate method to fabricate these Sb nanofilms by the epitaxial growth on the inert substrates for investigating their thickness-dependent intrinsic properties.[40–42]

In this article, we reported the successful fabrication of the Sb nanofilms of different thicknesses by a combination of epitaxial growth and controllable thermal desorption on the inert highly oriented pyrolytic graphite (HOPG) substrates. Firstly, we systematically studied the growth behaviors of Sb on HOPG at different substrate temperatures. The well-crystallized Sb nanofilms were obtained at 371 K with a thickness of $\sim$ 4–6 nm, and determined as β-Sb nanofilms by atomically STM measurements. The thinner Sb nanofilms of $\sim$ 2.2–3.5 nm were obtained by the sequentially thermal desorption of the top Sb layer. Two different forms of Moiré patterns on the Sb nanofilms were also observed by STM, which is due to the interlayer rotation of the top Sb layers and the introduction of thermal strain by the desorption process. The AFM lateral manipulation and surface potential measurements indicated that the Sb nanofilms on the HOPG substrate could be considered as the quasi-freestanding films due to the weak interfacial interaction and negligible charge transfer between them.

2. Experimental methods

Sample preparation and STM measurements Our growth experiment was carried out in an ultra-high vacuum (UHV) chamber with a base pressure of 3.0×10^{-10} Torr, equipped with standard MBE capabilities. The HOPG substrate was cleaved in air and immediately loaded into the MBE chamber, then annealed at 673 K overnight to remove contaminants. During growth, high purity Sb (99.999%) was evaporated from a Knudsen cell onto the substrate kept at various temperatures (from room temperature to 371 K). The growth process and crystal structure of the Sb nanofilm were *in situ* monitored and roughly revealed by the reflection high-energy electron diffraction (RHEED). After the growth experiment, the sample was first transferred to another UHV chamber with LT-STM (PanScan Freedom, RHK) for the following STM measurements and controllable thermal desorption at 473 K. All STM measurements were performed at 9 K with chemical etched W tip. Gwyddion software was used for STM data analysis.

AFM measurements AFM measurements were performed on a commercial AFM system (MFP-3D Infinity, Asylum Research), in combination with a dynamic signal analyzer (HF2LI, Zurich Instruments) in the atmosphere circumstance. The topography and surface potential images of the Sb nanofilms were obtained with normal tapping and KPFM modes. The AFM manipulation of the Sb nanofilms on HOPG was realized with contact mode.

SEM measurements After growth, the sample was firstly checked by SEM for the previous and convenient characterization of the sample morphology.

3. Results and discussion

In bulk, several allotropes exist for group V element at ambient condition due to their large number of valence electrons. According to the theoretical work by Wang *et al.*, four kinds of antimonene allotropes were confirmed, which are termed as α-, β-, γ-, and δ-Sb.[43] Only the α-Sb and β-Sb are relatively stable, which can be obtained by various experimental methods. The atomic structural configurations of α-Sb and β-Sb antimonene allotropes are shown in Fig. 1. The structure of α-Sb monolayer is similar to that of black phosphorus, which has a puckered rectangular lattice. The lattice constants of α-Sb are $a_1 = 4.77$ Å, $a_2 = 4.28$ Å, and $\theta_1 = 94.6°$, $\theta_2 = 103.5°$, respectively. The multilayer α-Sb is composed of AB stacked α-phase monolayer with a layer distance of 6.16 Å. The β-Sb monolayer has a hexagonal lattice with buckled bilayer structure with lattice constants of $a = 4.12$ Å and $\theta = 90.8°$. The multilayer β-Sb is composed of ABC stacked β-phase monolayer with a layer distance of 3.65 Å.

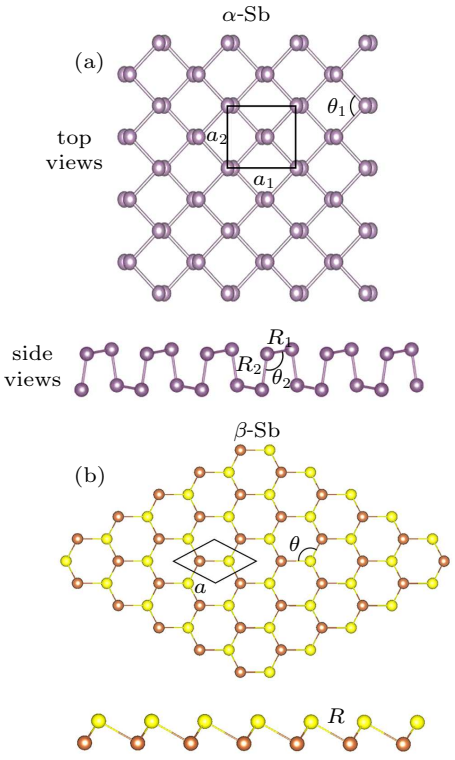


Fig. 1. Atomic structural models of antimonene allotropes. (a) Top view and side view of α-Sb. (b) Top view and side view of β-Sb.

According to the theoretical calculations, the α-Sb is structurally more stable than β-Sb for the thickness of less

than three layers, and will transform into β-Sb when the film thickness is larger three layers. The few-layered α-Sb nanofilms can be experimentally epitaxial grown on the lattice-matched substrate, like α-Bi substrate or film. The quasi-freestanding Sb nanofilms can be fabricated through vdW epitaxial growth on the inert substrates, while the experimentally obtained Sb nanofilms are relatively thick ($\sim$ 10 nm) due to the high coherent energy of Sb. The α-Sb monolayer is a topological trivial direct bandgap semiconductor with a band gap of 0.28 eV, while 2 ML α-Sb nanofilms were predicated to be topological non-trivial, belonging to the quantum spin Hall state class.[44] Recently, Zhang *et al.* have shown that the β-Sb nanofilms can undergo a series of topological transitions with decreasing thickness: from a topological semimetal to a topological insulator at 7.8 nm (22 layers), then a quantum spin Hall (QSH) phase at 2.7 nm (8 layers) and a topological trivial semiconductor at 1.0 nm (3 layers).[15] Here, we will mainly focus on the epitaxial growth and thickness-control of quasi-quasi-freestanding Sb nanofilms on the inert HOPG substrate, which is a prerequisite step to investigate their thickness-dependent topological properties.

Antimony was deposited by thermal deposition of the solid material and condensation of the vapor onto the HOPG substrate kept at different temperature. Figure 2 shows the general morphology, structural details, and topography of the Sb nanofilms with increasing substrate temperatures. When the substrate was kept at room temperature ($\sim$ 304 K), the fingerlike Sb structures were formed with lateral size of $\sim$ 10 μm, as shown in Fig. 2(a). Figure 2(b) shows a magnified SEM image of a typical fingerlike structure with six approximate 6-fold symmetric main branches. This kind of 6-fold symmetricity may result from the partially crystallization of the central part of the fingerlike structure. The trunk part of branches should also be crystalized, considering their similar contrast with the central part in the SEM images. The average thickness of these fingerlike structures is $\sim$ 40 nm, as shown in the AFM topography image of Fig. 2(c). The crystalized parts of the fingerlike structures are several nanometers lower than the round amorphous parts at the edges of the branches. This kind of crystallization is driven by a size dependent amorphous to crystalline phase transition, similar to ice crystal formation from supercooled water droplets.[45,46]

When the substrate temperature was increased to $\sim$ 314 K, the flower-shaped Sb nanofilms were formed with lateral size of 10–15 μm, as shown in Fig. 2(d). Figure 2(e) shows a magnified SEM image of a typical flower-shaped Sb nanofilm with smoothly curved edges, indicating their amorphous nature. The average thickness of these fingerlike structures is 8–10 nm, as shown in the AFM topography image of Fig. 2(f). It is noted that there are many small triangular nanofilms on their surface. We can conclude that the crystallization process has been started from the surface layers of the amorphous flower-shaped structures at $\sim$ 314 K.

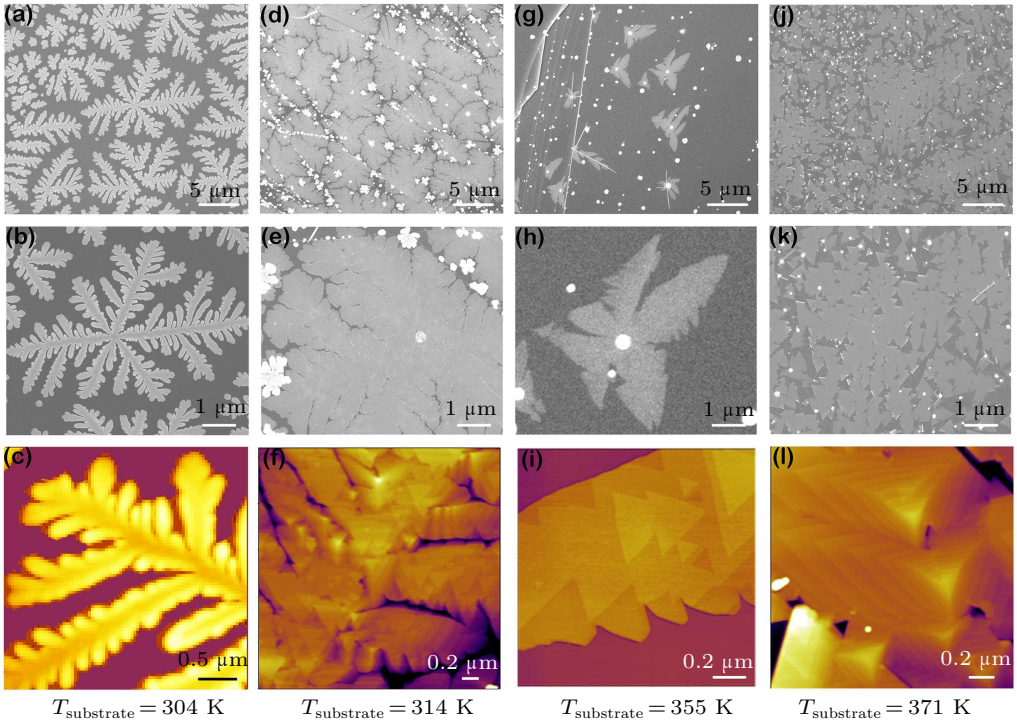


Fig. 2. Epitaxial growth of the Sb nanofilms on HOPG substrates at various temperatures. The HOPG substrate was kept at 304 K (a)–(c), 314 K (d)–(f), 355 K (g)–(i), and 371 K (j)–(l) respectively during growth. (a), (d), (g), (j) Large-scale SEM images show the general morphology of Sb nanofilms. (b), (e), (g), (k) The zoom in SEM images show more structural details of Sb nanofilms. (c), (f), (i), (l) AFM topography images show the thickness of Sb nanofilms.

When the substrate temperature was further increased to ∼ 355 K, the butterfly-shaped Sb nanofilms were formed with various lateral sizes, as shown in Fig. 2(g). Figure 2(h) shows a magnified SEM image of a typical butterfly-shaped Sb nanofilm with both smoothly curved edges and straight edges, indicating their further crystallization in comparison with those at ∼ 314 K. The average thickness of these butterfly-shaped structures is 4–6 nm, as shown in the AFM topography image of Fig. 2(i). The triangular nanofilms formed on their surface become larger and more extensive, indicating the further crystallization process at ∼ 355 K. It can also observe that the coverage of Sb nanofilms was relatively low, which is due to the decreased adhesion coefficient of Sb at the higher substrate temperature.

When the substrate temperature reached 371 K, the triangle-shaped Sb nanofilms were formed, as shown in Fig. 2(j). Figure 2(k) shows a magnified SEM image of typical triangle-shaped Sb nanofilms, indicating their complete crystallization. It is also noted that these triangle-shaped Sb nanofilms show various different orientations, which is due to the weak interfacial interactions between the Sb nanofilms and the inert HOPG substrate. The average thickness of these triangle-shaped structures is 4–6 nm, as shown in the AFM topography image of Fig. 2(l). The triangular Sb nanofilms prefer to grow in a three-dimensional way, and form connected thick islands. In the next part, these crystalized Sb nanofilms will be mainly investigated, including their atomic structures and thermal-desorption behaviors.

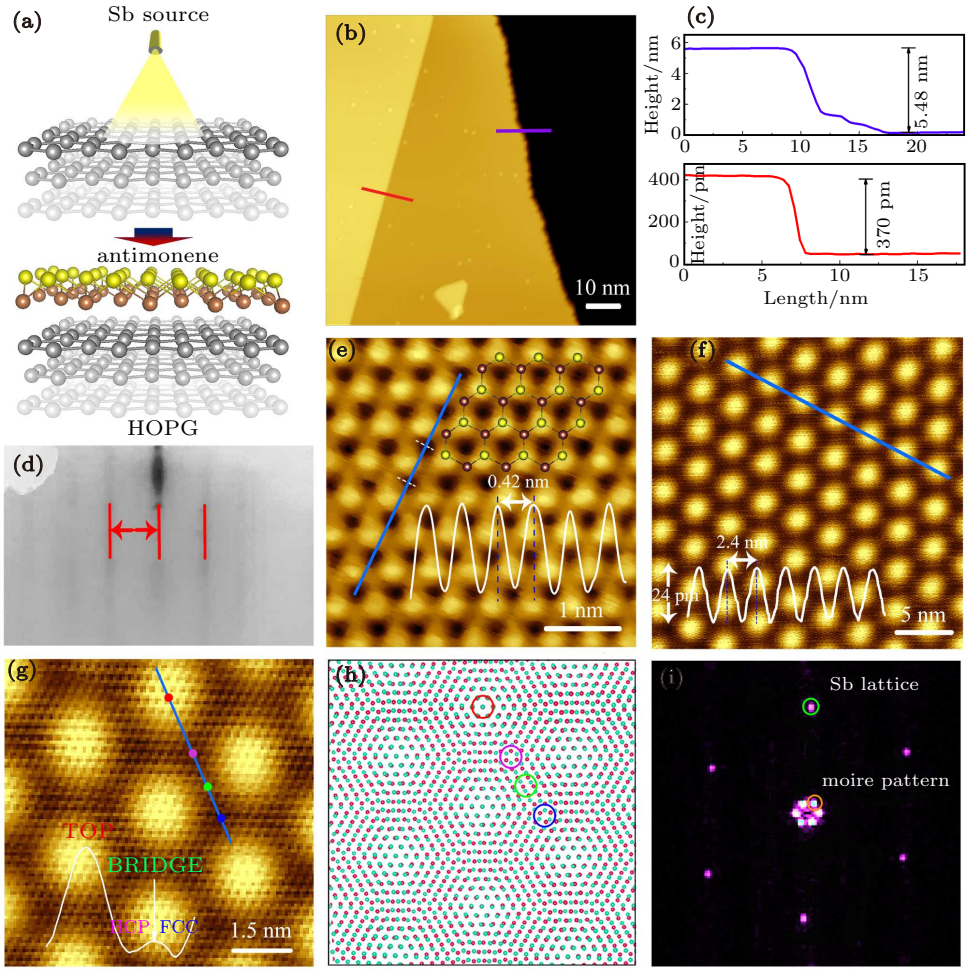


Fig. 3. STM measurements of the β-Sb nanofilm on HOPG. (a) Schematic of the deposition process. (b) STM topographic image ($V_t = 2.1$ V, $I_t = 400$ pA) of the Sb nanofilm with the edges. (c) The height line profiles show the thickness (purple) and single step height (red) of the Sb nanofilm, respectively. (d) RHEED pattern of the Sb nanofilm on HOPG. (e) Atomic resolution STM image ($V_t = -1.4$ V, $I_t = 700$ pA) of Sb nanofilm with the overlaid atomic structural model. Inset: line profile along the blue line, showing the periodicity of β-Sb lattice (4.2 Å). (f) STM image of the Moiré pattern was occasionally observed ($V_t = 2.4$ V, $I_t = 300$ pA) in Sb nanofilms. The insert line profile presents the period and amplitude of the Moiré pattern. (g) Atomic resolution image of (f) ($V_t = 2.4$ V, $I_t = 300$ pA,). (h) Schematic structural model of (g). The high symmetric sites are marked by the corresponding color circles in (h) and dots in (g): TOP (red), HCP (purple), BRIDGE (green), and FCC (blue). (i) FFT of the atomic resolution image of (g).

The STM measurements were performed on the crystallized Sb nanofilms, as shown in Fig. 3. Figure 3(a) is the schematic of the deposition process of Sb on HOPG substrate. Figure 3(b) shows a large-scale STM topography image of Sb nanofilms on HOPG substrate with the edges. As shown in Fig. 3(c), the thickness of the Sb nanofilm was 5.48 nm

(marked by the purple line in Fig. 3(b)), which is within the height range of topological insulator (7.8 nm $> h >$ 2.7 nm). The single step height of the Sb nanofilm is measured to be 0.37 nm (marked by the red line in Fig. 3(b)), which is consistent with the theoretical thickness of a β-Sb monolayer. In comparison with the straight step edges of the top layer, the thick edges of the nanofilms are corrugated, which should be related with their special growth process, as shown in Fig. 2. The RHEED pattern of the Sb nanofilm is shown in Fig. 3(d). By a comparison with the RHEED pattern of HOPG substrate, the ratio of the stripe spacing $d_{\mathrm{Sb}}/d_{\mathrm{HOPG}} = 1.833$ is obtained (the RHEED pattern of HOPG does not present here). This value is roughly consistent with the theoretical result $d_{\beta-\mathrm{Sb}}/d_{\mathrm{HOPG}} = 1.706$, indicating that the Sb nanofilms belong to β-Sb. The atomic resolution image of the Sb nanofilms is shown in Fig. 3(e), where the bright and dark balls of the overlaid model represent the upward and downward Sb atoms of the buckled honeycomb structure, respectively. The lattice constant is measured to be $\sim$ 0.42 nm, which is in agreement with the parameter of previously reported β-Sb.[9]

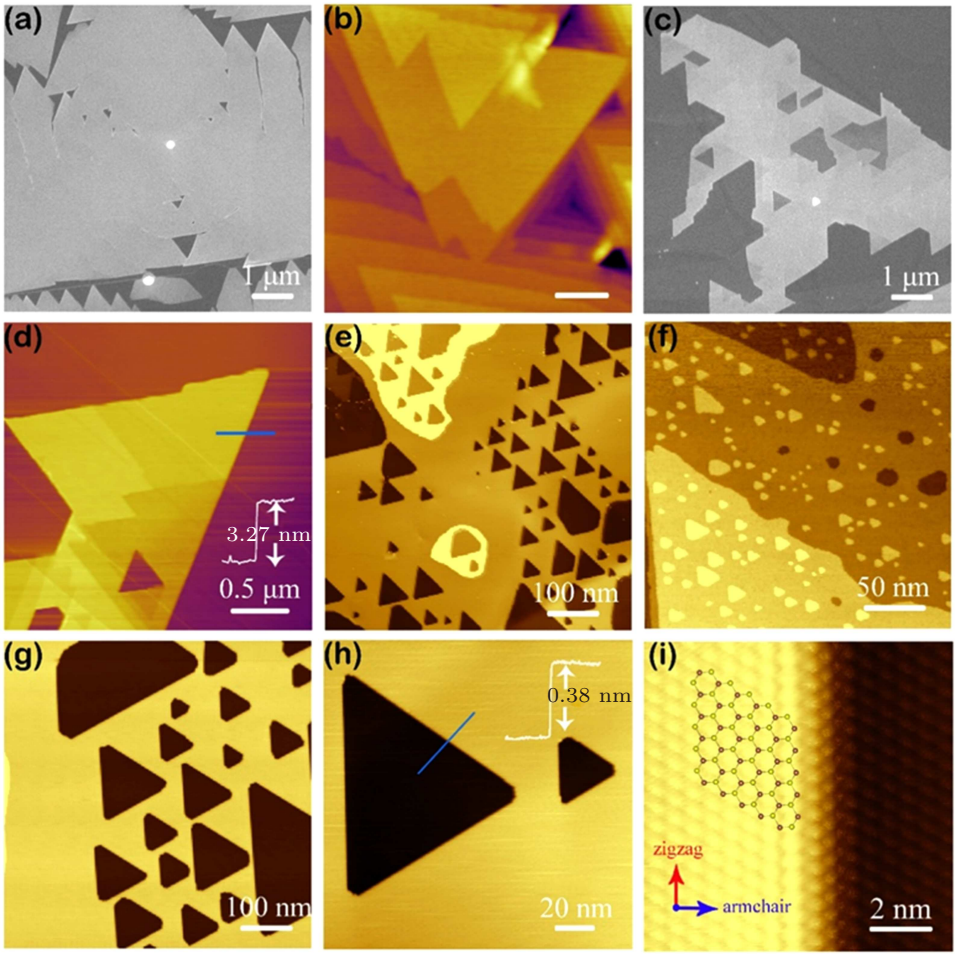


Fig. 4. Thermal desorption to control the thickness of Sb nanofilms. (a) and (b) SEM image and AFM image of the Sb nanofilm before desorption, respectively. (c) and (d) SEM image and AFM image of the Sb nanofilm after desorption, respectively. The height line profile shows the thickness of the desorbed Sb nanofilms at $\sim$ 3.27 nm. (e) Large-scale STM topographic image of Sb nanofilm after thermal desorption. The Sb nanofilm has been partially desorbed ($V_{\mathrm{t}} = 2.14$ V, $I_{\mathrm{t}} = 300$ pA). (f) During the desorption, the Sb atoms can redeposit to form small triangular islands ($V_{\mathrm{t}} = -2.4$ V, $I_{\mathrm{t}} = 150$ pA). STM images (g) and (h) reveal that many triangular holes are formed on the surface of the desorbed Sb nanofilm ($V_{\mathrm{t}} = 2.0$ V, $I_{\mathrm{t}} = 100$ pA). (i) Atomic resolution at step edge of the triangular hole. The atomic structural model of β-Sb is superimposed on the step edge ($V_{\mathrm{t}} = 0.1$ V, $I_{\mathrm{t}} = 800$ pA).

The regularly arranged dot-like Moiré patterns can be occasionally observed on the Sb nanofilm (Fig. 3(f)). The period of the Moiré pattern is 2.4 nm, and the amplitude is 24 pm (as shown by the overlaid line profile). It is noted that the period of the supercell of Moiré patterns is close to 6 times the size of Sb lattice constant (the lattice constant of β-Sb is 0.42 nm). According to the previous work, this type of Moiré pattern should be due to the small rotation between two top layers of antimonene. The rotation angle of $\sim 6^{\circ}$ was further determined by the atomic resolution of the Moiré pattern, as shown in Fig. 3(g). Figure 3(h) shows the schematic structural model obtained by stacking two β-Sb monolayers with a rotating angle of 6°. The structural details of the model are in agreement with the atomic resolution image of the Moiré pattern. The high symmetric sites of TOP, HCP, BRIDGE, and FCC within one Moiré supercell were marked on the blue line.

The height difference between ATOP (red dot) and HCP (purple dot) is 25 pm, between HCP and BRIDGE (green dot) is 3 pm, and between BRIDGE and FCC (blue dot) is 4 pm. Fast Fourier transformation (FFT) of Fig. 3(g) presents two sets of hexagonal reciprocal lattice points, as shown in Fig. 3(i). The six points close to the center obviously correspond to the large Moiré pattern, and the other set of points correspond to the lattice of β-Sb. The rotation angle of $\sim 6^\circ$ was also calculated by the two sets of FFT points, further confirming the proposed model in Fig. 3(h).

By increasing the deposition time, the thicker crystalized β-Sb nanofilms can be obtained, which is within the range of topological semimetal ($h > 7.8$ nm). While no thinner crystalized β-Sb nanofilms can be obtained by a direct deposition process in our experiments. In the next, we proposed a controllable thermal desorption method[47–49] to get the thinner crystalized β-Sb nanofilms. At low coverages, most of the Sb nanofilms are amorphous or partially crystalized. During the desorption process, no crystallization but direct desorption process happened within these nanofilms. The thinner crystalized nanofilms can only be obtained from the thicker crystalized nanofilms through controllable thermal desorption.

Figure 4(a) shows the SEM morphology image with high coverage Sb nanofilms before desorption. The triangular Sb nanofilms grow in a three-dimensional way, and form connected thick nanofilm islands, as show in Fig. 4(b). Figure 4(c) shows the SEM morphology image after desorption at 513 K. The coverage and thickness of the Sb nanofilms were clearly decreased, some large regular holes can be observed within the nanofilms. The thinner Sb nanofilms with a thickness of ~ 3.5 nm to 2.2 nm (6–10 layers of antimonene) were obtained, as shown in Fig. 4(d), which is of great significance for further studying the state transition from topological insulator to two-dimensional quantum spin state.

STM measurements presented more structural details of the desorbed Sb nanofilms. Figure 4(e) is a large-scale STM topographic image of the Sb nanofilms after thermal desorption, where many triangular holes of different sizes are observed on the top of the nanofilms. Both holes and islands were observed on some Sb nanofims, as shown in Fig. 4(f), indicating that the desorbed Sb atoms can redeposit back to form many small triangular islands. These triangular holes show straight edges and rough vertices, as shown in Fig. 4(g), where these vertices should be the active desorption sites. The depths of all these triangular holes are a single step height of ~ 0.38 nm, as shown in Fig. 4(h), indicating a possible mechanism of single top layer desorption. Figure 4(i) shows the atomic resolution images of the triangular hole across the edge, where the atomic structural model of β-Sb is overlaid along the step edge. According to the model, the edges are determined to be along the zigzag direction with buckled down Sb atoms at the outmost. This kind of edges is relatively stable, while the vertices are considered to be made of unstable edges with buckled down Sb atoms at the outmost. So the vertices of the triangular holes should be the active desorption sites.

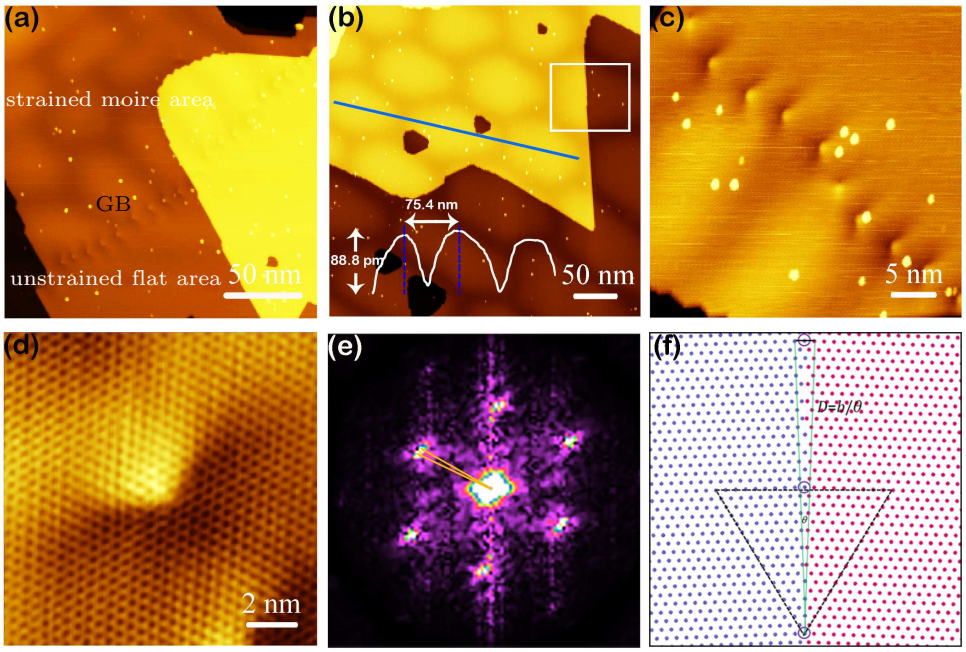


Fig. 5. Strained Moiré superstructures of the Sb nanofilms after thermal desorption. (a) and (b) STM images of Moiré pattern by the thermal strain during the desorption ($V_t = 2.4$ V, $I_t = 200$ pA). The grain boundaries (GBs) separate the strained Moiré area and unstrained flat area of Sb nanofilms. (c) The magnified image at the grain step edge. (d) Atomic resolution image of the dislocation ($V_t = 0.2$ V, $I_t = 400$ pA). (e) FFT of the atomic resolution image of (d). (f) Schematic model of the dislocation of a 4° GB. ($D = b/\theta$, and $\theta = \tan^{-1}(1/(\sqrt{3}(2n+1)))$, $n = 8$ here).

Another kind of huge Moiré superstructure was also observed, which is due to the introduction of thermal strain during the desorption process. The strained Moiré areas and unstrained flat areas were observed on the nanofilms, which were separated by through grain boundaries (GB), as shown in Fig. 5(a). The period of the strained Moiré superstructures is 75.4 nm (Fig. 5(b)), and the amplitude is 88.8 pm, which is much larger than the Sb lattice constant. The Moiré superstructures can span the steps of Sb nanofilms (as marked by rectangle in Fig. 5(b)), indicating the effect of thermal strain is not limited to the top layer of Sb nanofilms. The grain boundaries were made of periodical dislocations (Fig. 5(c)), indicating the in-plane rotation between the strained Moiré area and unstrained flat area.[50] Figure 5(d) shows the atomic resolution image of a typical dislocation. The angle (θ) of in-plane rotation can be directly determined from the FFT of Fig. 5(d), which is measured to be $\sim 4^\circ$ between two sets of β-Sb reciprocal lattice points in Fig. 5(e). Figure 5(f) shows the schematic diagram of the dislocation model of a $\sim 4^\circ$ GB, where $D = b/\theta$ and $\theta = \tan^{-1}(1/(\sqrt{3}(2n+1)))$ ($n = 8$ here). The in-plane strain around the dislocations could be used to tune the topological states of Sb nanofilms, which is worthy of further investigation.

The interfacial interaction between the Sb nanofilm and HOPG substrate was further studied by lateral AFM manipulation and surface potential measurements with KPFM. Figure 6(a) is schematic diagram of Sb nanofilms manipulated by AFM tip in contact mode. Figures 6(b) and 6(c) show the AFM images of the Sb nanofilm before and after the manipulation. One branch of the Sb nanofilm was broken and moved on the HOPG substrate, which indicates that the interfacial interaction between the Sb nanofilm and HOPG substrate is relatively weak. The corresponding surface potential image was obtained by KPFM measurement, as shown in Fig. 6(d). The surface potential of Sb nanofilms is $\sim$ 120 mV higher that of HOPG, as shown in Fig. 6(e). This difference is roughly consistent with their work functions (HOPG: 4.6 eV; Sb: 4.55 eV), which means there is no significant charge transfer between the Sb nanofilms and HOPG substrate. It can be concluded that the Sb nanofilms grown on HOPG can be assumed at the quasi-freestanding condition.

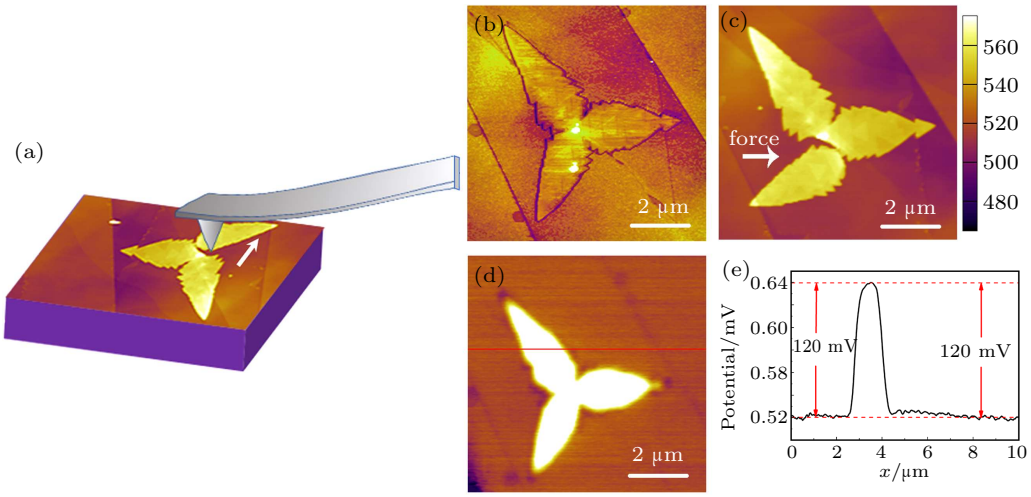


Fig. 6. Interfacial interactions and surface potential of the epitaxial Sb nanofilm on HOPG substrate. (a) Schematic diagram of Sb nanofilms manipulated by AFM tip in contact mode. (b) AFM image of the Sb nanofilm on HOPG. After the manipulation, the part of the Sb nanofilm was broken and moved on HOPG surface, as shown in the following AFM image of (c). (d) The corresponding surface potential image of (b) obtained by KPFM measurement. (e) The surface potential difference between Sb nanofilm and HOPG substrate is $\sim$ 120 mV, as shown in the line profile in (d).

4. Conclusion

In summary, the Sb nanofilms of different thicknesses have been successfully fabricated by a combination of epitaxial growth and controllable thermal desorption on the inert HOPG substrates. These Sb nanofilms can be assumed as the quasi-freestanding films due to the weak interfacial interactions. The in-plane strain can also be introduced to affect the topography and properties of these nanofilms by the thermal desorption. It will be our next work to further investigate the thickness-dependent topological characteristics of these Sb nanofilms.

References

[1] Zhang S L, Guo S Y, Chen Z F, Wang Y L, Gao H J, Gomez-Herrero J, Ares P, Zamora F, Zhu Z and Zeng H B 2018 *Chem. Soc. Rev.* **47** 982
[2] Feng B J, Zhang J, Zhong Q, Li W B, Li S, Li H, Cheng P, Meng S, Chen L and Wu K H 2016 *Nat. Chem.* **8** 563
[3] Qin Z H, Pan J B, Lu S Z, Yan S, Wang Y L, Du S X, Gao H J and Cao G Y 2017 *Adv. Mater.* **29** 1606046
[4] Meng L, Wang Y L, Zhang L Z, Du S X, Wu R T, Li L F, Zhang Y, Li G, Zhou H T, Hofer W A and Gao H J 2013 *Nano Lett.* **13** 685
[5] Zhang J L, Zhao S T, Han C, Wang Z Z, Zhong S, Sun S, Guo R, Zhou X, Gu C D, Yuan K D, Li Z Y and Chen W 2016 *Nano Lett.* **16** 4903
[6] Lu N D, Wang L F, Li L and Liu M 2017 *Chin. Phys. B* **26** 036804
[7] Yang J and Lu Y R 2017 *Chin. Phys. B* **26** 034201
[8] Huang X C, Guan J Q, Lin Z J, Liu B, Xing S Y, Wang W H and Guo J D 2017 *Nano Lett.* **17** 4619

[9] Wu X, Shao Y, Liu H, Feng Z, Wang Y L, Sun J T, Liu C, Wang J O, Liu Z L, Zhu S Y, Wang Y Q, Du S X, Shi Y G, Ibrahim K and Gao H J 2017 *Adv. Mater.* **29** 1605407

[10] Reis F, Li G, Dudy L, Bauernfeind M, Glass S, Hanke W, Thomale R, Schafer R and Claessen R 2017 *Science* **357** 287

[11] Li K L, Yu Y J, Ye G J, Ge Q Q, Ou X D, Wu H, Feng D L and Chen X H 2014 *Nat. Nanotechnol* **9** 372

[12] Sugawara K, Sato T, Souma S, Takahashi T, Arai M and Sasaki T 2006 *Phys. Rev. Lett.* **96** 046411

[13] Hsieh D, Xia Y, Wray L, Qian D, Pal A, Dil J H, Osterwalder J, Meier F, Bihlmayer G, Kane C L, Hor Y S, Cava J R and Hasan M Z 2009 *Science* **323** 919

[14] Seo J, Roushan P, Beidenkopf H, Hor Y S, Cava J R and Yazdani A 2010 *Nature* **466** 343

[15] Zhang P F, Liu Z, Duan W H, Liu F and Wu J 2012 *Phys. Rev. B* **85** 201410

[16] Ares P, Zamora F and Gomez-Herrero J 2017 *Acs Photon.* **4** 600

[17] Gibaja C, Rodriguez-San-Miguel D, Ares P, Gomez-Herrero J, Varela M, Gillen R, Maultzsch J, Hauke F, Hirsch A, Abellan G and Zamora F 2016 *Angew. Chem. Int. Edit* **55** 14345

[18] Sun X, Lu Z H, Xiang Y, Wang Y P, Shi J, Wang G C, Washington M A and Lu M T 2018 *ACS Nano* **12** 6100

[19] Dai X Y, Jin G Q, Dong J Q, Wang C B, Zhao X, Chu Y P, Xi P C, Deng W H, Zhang H M and He Y 2011 *Acta Phys. Sin.* **60** 065101 (in Chinese)

[20] Qiu Y F, Du H W and Wang B 2011 *Acta Phys. Sin.* **60** 036801 (in Chinese)

[21] Panahi N, Hosseinnejad M T, Shirazi M and Ghoranneviss M 2016 *Chin. Phys. Lett.* **33** 066802

[22] Liu S J, He Y F, Wei H Y, Qiu P, Song W M, An Y L, Rehman A, Peng M Z and Zheng X H 2019 *Chin. Phys. Lett.* **28** 026801

[23] Lan W, Tang G M, Cao W L, Liu X Q and Wang Y Y 2009 *Acta Phys. Sin.* **58** 8501 (in Chinese)

[24] Yu L H, Xue A J, Dong S T and Xu J H 2010 *Acta Phys. Sin.* **59** 4150 (in Chinese)

[25] Sun B, Chang H D, Lu L, Liu H G and Wu D X 2012 *Chin. Phys. Lett.* **29** 036102

[26] Su S J, Wang W and Zhang G Z 2011 *Acta Phys. Sin.* **60** 028101 (in Chinese)

[27] Lei T, Liu C, Zhao J L, Li J M, Li Y P, Wang J O, Wu R, Qian H J, Wang H Q and Ibrahim K 2016 *J. Appl. Phys.* **119** 015302

[28] Fortin-Deschenes M, Waller O, Mentes T O, Locatelli A, Mukherjee S, Genuzio F, Levesque P L, Hebert A, Martel R and Moutanabbir O 2017 *Nano Lett.* **17** 4970

[29] Shao Y, Liu Z L, Cheng C, Wu X, Liu H, Liu C, Wang J O, Zhu S Y, Wang Y Q, Shi D X, Ibrahim K, Sun J T, Wang Y L and Gao H J 2018 *Nano Lett.* **18** 2133

[30] Yao G G, Luo Z Y, Pan F, Xu W T, Feng P Y and Wang X S 2013 *Sci. Rep.* **3** 2010

[31] Kim S H, K Jin K H, Park J, Kim J S, Jhi S H and Yeom H W 2016 *Sci. Rep.* **6** 33193

[32] Luo Z F, Wu Z M, Xu X D, Wang T and Jiang X D 2011 *Acta Phys. Sin.* **60** 067302 (in Chinese)

[33] Meng X Q, Fang Y Z and Wu F M 2012 *Chin. Phys. Lett.* **29** 016801

[34] Liu X J, Cao W Q, Huang Z H, Yuan J, Fang X Y and Gao M S 2015 *Chin. Phys. Lett.* **32** 036802

[35] Yang J J, Fang Q Q, Du W H, Zhang K K and Dong D S 2018 *Chin. Phys. B* **27** 037804

[36] Zhu C F, Sha X, Chu X Y, Li J H, Xu M Z, Jin F J and Xu Z K 2018 *Chin. Phys. B* **27** 027803

[37] He X M, Chen Z M and Li L B 2015 *Chin. Phys. Lett.* **32** 036801

[38] Shi X M, Wang G Y, Wang R F, Zhou X Y, Xu J T, Tang J and Ang R 2018 *Chin. Phys. B* **27** 047204

[39] Tan M R, Liu Q H, Sui N, Kang Z H, Zhang L Q, Zhang H Z, Wang W Q, Zhou Q and Wang Y H 2019 *Chin. Phys. B* **28** 056106

[40] Shen K C, Hua C Q, Liang Z F, Wang Y, Sun H L, Hu J P, Zhang H, Li H Y, Jiang Z, Huang H, Wang P, Sun Z, Wahlström E, Lu Y H and Song F 2019 *ACS Appl. Electron. Mater.* **1** 1817

[41] Song F, Wells J W, Jiang Z, Saxegaard M and Wahlström 2015 *EACS Appl. Mater. Interfaces* **7** 8525

[42] Yang Z Q, Jia J F and Dong Qian D 2016 *Chin. Phys. B* **25** 117312

[43] Wang G X, Pandey P and Karna S P 2015 *Acs Appl. Mater. Inter* **7** 11490

[44] Märkl T, Kowalczyk P J, Ster M L, Mahajan I V, Pirie H, Ahmed Z, Bian G, Wang X, Chiang T C and Brown S A 2018 *2D Mater.* **5** 011002

[45] Stegemann B, Ritter C, Kaiser B and Rademann K 2004 *J. Phys. Chem. B* **108** 14292

[46] Kaiser B, Stegemann B, Kaukel H and Rademann K 2002 *Surf. Sci.* **496** L18-L22

[47] Shen K C, Hua C Q, Liang Z F, Wang Y, Sun H L, Hu J P, Zhang H, Li H Y, Jiang Z, Huang H, Wang P, Sun Z, Wahlstrom E, Lu Y H and Son F 2019 *ACS Appl. Electron. Mater* **1** 1817

[48] Feng X X, Liu N X, Zhang N, Wei T B, Wang J X and Li J M 2014 *Chin. Phys. Lett.* **31** 056801

[49] Luo J X, Chen J, Chai Z, Lv K, He W W, Yang Y and Wang X 2014 *Chin. Phys. Lett.* **31** 126601

[50] Liu Y, Li Y Y, Rajput S, Gilks D, Lari L, Galindo P L, Weinert M, Lazarov V K and Li L 2014 *Nat. Phys.* **10** 294